ORIGINAL ARTICLE

Mission Design for the 2020 Mercury Lander Decadal Survey

Jackson L. Shannon[1] (ORCID) · **Justin A. Atchison[1]** · **Benjamin F. Villac[1]** · **Gabe Rogers[1]** · **Martin T. Ozimek[1]**

Abstract

This paper presents the mission design for a Mercury Lander concept in support of NASA's 2020 Planetary Science Decadal Survey. We evaluated both chemical and solar electric propulsion trajectory options for the interplanetary and orbital phases. Like previous missions, our solution uses a series of Venus and Mercury gravity assists to reduce the total delta-V needed to capture at Mercury. Solar electric propulsion offers significant propellant savings for the interplanetary phases, but results in unreasonably long flight times during the orbital lowering phase. Based on these trades, we selected a trajectory that uses a NEXT-C electric propulsion system with a baseline power of 9 kW to orbit match with Mercury. Upon arrival at Mercury, the electric propulsion stage is jettisoned, and a chemical system performs orbit insertion and lowering to the final orbit. Descent and landing are performed using a solid rocket motor and liquid propulsion system, respectively. The arrival is phased so that the lander can operate in local nighttime for up to 13 weeks, with direct-to-Earth communication availability for up to 7 weeks.

Introduction

The MESSENGER mission mapped Mercury and identified a variety of new questions, including the source of large regions of volatile-rich composition [1]. A

✉ Jackson L. Shannon
  Jackson.Shannon@jhuapl.edu

[1] Astrodynamics and Controls Group, Space Exploration Sector, Johns Hopkins Applied Physics Laboratory, 11100 Johns Hopkins Rd, Laurel, MD 20723, USA

Mercury Lander mission would provide *in-situ* measurements of these regions to study this geochemistry, as well as the core's structure and magnetic field. The scientific merit of these measurements motivated a mission study for NASA's 2020 Planetary Science Decadal Survey [2].

This paper describes the mission design associated with this concept. The spacecraft has four stages: cruise, orbit, descent, and landing. We evaluated chemical and solar electric propulsion (SEP) options for both the interplanetary transfer and the orbital transfer after capture at Mercury. For the interplanetary transfer, our approach was to first develop an optimal impulsive minimum ΔV interplanetary transfer that captured at Mercury, and then evaluate the potential propellant savings from converting the impulsive maneuvers to SEP thrust arcs. Once captured at Mercury, we then considered both chemical and SEP trajectories to descend into a stable low-energy orbit, from which the descent and landing stages would initiate. Figure 1 illustrates the various mission design choices that were considered for this mission. The shaded boxes indicate the options selected.

Thermal challenges associated with the low solar distances presented the largest constraints and drivers for the mission design process. Despite the substantial increase in available power for SEP at low solar distances, the spacecraft solar arrays must be off-pointed to maintain an operable temperature. Additionally, the increased solar irradiation causes the arrays to degrade faster than missions that operate at 1 AU or further. The result is a relatively large solar array required to achieve an efficient transfer. Based on this, our SEP selection minimizes the total system mass by using the smallest power system that achieves the required ΔV.

Thermal considerations also place a constraint on any available SEP thrust vector pointing. A Sun shade is used to limit the spacecraft temperature. Based on its size,
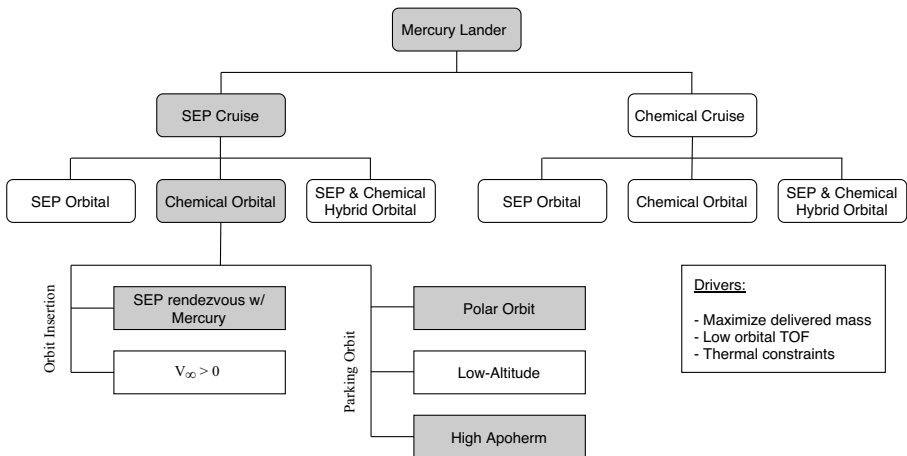

Fig. 1 Tree of mission design options for the interplanetary and orbital mission phases
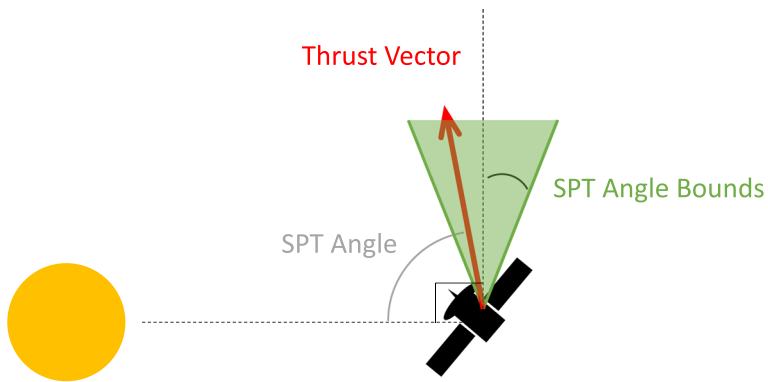
Fig. 2 SPT angle constraint

the spacecraft can never point more than 15° away from the plane normal to the Sun-line. Accounting for practical attitude variation, this constrains the Sun-Probe-Thrust (SPT) angle to have a tolerance of 90° ± 10°. A diagram of this constraint is shown if Fig. 2.

The final design delivers 620 kg of Lander dry mass to the Mercury surface. The trajectory leverages a fully expendable Falcon Heavy launch vehicle and uses SEP to orbit match with Mercury after a series of Venus and Mercury gravity assists. A chemical system inserts the spacecraft into a thermally stable parking orbit and then performs orbit lowering before descent operations begin. The descent sequence uses a solid rocket motor to eliminate most of the spacecraft's kinetic energy. A liquid propulsion system on the lander adds additional maneuverability and performs the final burns for a soft landing. During this phase, hazard detection is performed and a landing site is chosen through scanning LIDAR measurements. Landing is timed to occur just hours prior to local nighttime. To maintain a survivable temperature, the lander operates using a radioisotope thermal generator during the nighttime period, with periods of communication availability directly to Earth. The mission ends 13 weeks later when local daytime returns and the heat flux exceeds the lander's survivable range.

Impulsive Maneuver Transfer Search

We first searched for low ΔV impulsive interplanetary transfers from Earth to Mercury rendezvous. This transfer is complicated by Mercury's short period, eccentric (0.2), and inclined (7 deg) orbit relative to the ecliptic. As previous studies [3, 4], NASA's MESSENGER mission [5], and ESA's Bepicolombo mission [6, 7] found, an efficient transfer uses a series of Venus and Mercury gravity assists and v-infinity leveraging maneuvers (VILMs) to orbit match with Mercury. This approach trades ΔV with flight time, and requires the right phasing of Earth, Venus, and Mercury.

(a) Earth-Venus-Venus-Mercury launch opportunities.

(b) Effect of transfer orbit orientation on v-infinity.
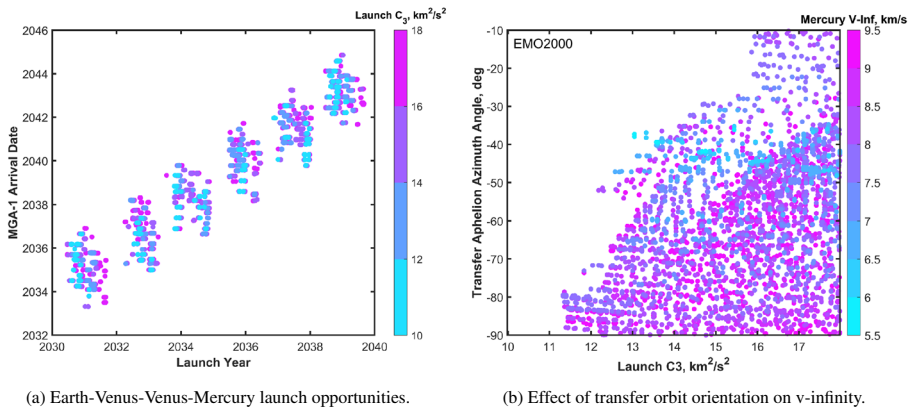
Fig. 3 Broad ballistic search results

To identify viable launch dates, we followed the process outlined by Yen [3]. We used one or two Venus gravity assists (VGA) to lower the spacecraft's perihelion to Mercury's orbit near perihelion and align the spacecraft's line-of-apsides into a favorable orientation. Following the synodic period of Venus, there are Earth-Venus-Venus-Mercury (EVVM) launch opportunities of about a year, followed by an approximately 7 month gap before the next opportunity, as shown in Fig. 3a. We found that a favorable orientation for a Mercury rendezvous can be quantified by an initial transfer aphelion that is "clockwise" tens of degrees from Mercury's aphelion, as shown in Fig. 3b. This angle is azimuth of the aphelion vector for the pre-Mercury encounter transfer, measured in the mean ecliptic (EMO2000) frame. Angles in the range of -60° to -30° had high likelihoods of offering low ΔV transfers. The first Mercury gravity assist (MGA) lowers the spacecraft aphelion to a 2:3 resonant period (3 Mercury periods to 2 spacecraft periods). Prior to the first MGA, the transfer is ballistic.

Figure 4 shows the minimal C3 and MGA_1 arrival v-infinity Pareto front for each launch opportunity grouping in Fig. 3a. The dashed line depicts the optimal phase-free ballistic MGA_1 arrival v-infinity (5.7 km/s) identified by Yen [3] for this encounter sequence. The x shows the corresponding minimum phase-free C3 at which this arrival condition can be achieved (17.64 km^2/s^2). The 2036 opportunity nearly achieves this optimal phasing, with a minimum MGA_1 arrival v-infinity of 5.78 km/s.

Following the first MGA, we use a series of VILMs to progressively lower each subsequent MGA v-infinity. This process shifts the flyby point closer to Mercury's perihelion and aligns the spacecraft's line-of-apsides with Mercury's line-of-apsides. The first MGAs match the orbit plane of Mercury. We initially focused on the favorable 2036 candidate, identifying a favorable 6 year solution with the following sequence of resonances: 2:3, 3:4, 5:6, 1:1. By further adding a second 3:4 resonance (2:3, 3:4, 3:4, 5:6, 1:1), we were able to reduce the overall delta-v (sum of cruise and arrival v-infinity) by roughly 170 m/s at the expense of an additional year of flight time. This extended sequence was used for the other successful launch cases. The
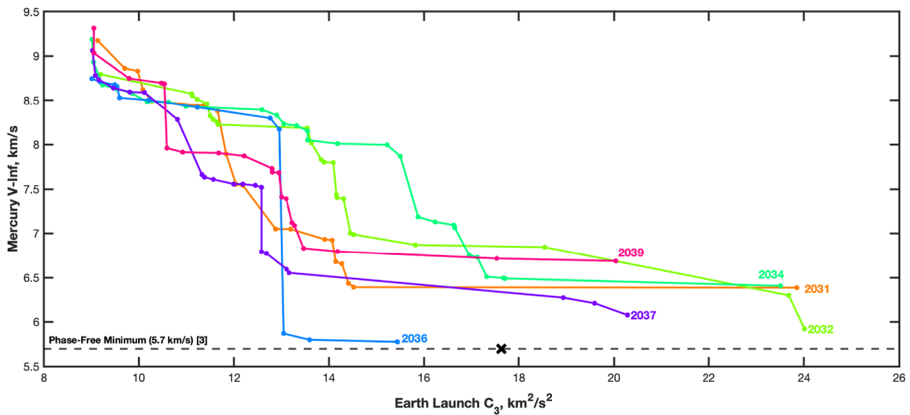
Fig. 4 Launch opportunity C3 and MGA$_1$ arrival v-infinity Pareto fronts

VILMs are modeled to be purely in the velocity direction at aphelion. We used the Explore tool [8], which implements a VILM search by varying the outgoing post-MGA true anomaly and the total time-of-flight [9]. It then solves for the ΔV required, if feasible, to re-encounter Mercury. We were unable to find any favorable sequences for the 2034 and 2039 launch opportunities, though this could indicate a limitation in our design process rather than a lack of competitive options.

For a given launch date, the search space consists of encounter dates and VILM parameters. The series of MGAs and VILMs has many physically realizable options, so as the gravity assist sequence is increased, the search becomes too large to be computationally reasonable on a standard PC. Typically, a Tisserand plot would be used to prune the sequence search space using encounter v-infinity and post gravity assist period. However, Mercury's eccentricity and inclination invalidate the standard Tisserand plot assumptions of coplanar circular orbits. Our approach to reduce the computational search time was to prune each leg's results using a Pareto filter that minimizes Mercury v-infinity and spacecraft VILM ΔV, keeping up to 1200 solutions after each MGA.

Table 1 presents our ballistic candidates starting from 2030. As points of comparison, the MESSENGER [5] and 2010 Decadal Survey [10] trajectories are included. The best opportunity launches in March of 2036 with two VGAs prior to the first MGA. Its ΔV and time-of-flight are comparable to these former cases. Figure 5 shows this trajectory in the ecliptic (EMO2000) frame. Despite different encounter dates, the trajectory after the second Venus swingby looks remarkably similar to Fig. 1 in Ref. [7].

Although this trajectory is consistent with the MESSENGER mission which successfully operated in Mercury orbit, the lander mission requirements are more challenging. Once at Mercury, the spacecraft must execute a descent and landing braking phase requiring over 4 km/s. That ΔV must be supplied for a lander payload that is more massive than the MESSENGER spacecraft dry mass. When these are accounted for, there is no practical implementation of a chemical ΔV lander mission.

Table 1 Comparison of impulsive mercury interplanetary transfers

| Case	Launch C3 (km^2/s^2)	Cruise ΔV (km/s)	Arrival V_{inf} (km/s)	Total Time of Flight (yr)
MESSENGER	16.40	1.08	2.20	6.6
2010 Decadal Survey	16.50	1.24	1.49	5.1
2031 Launch	13.02	2.99	3.90	8.9
2032 Launch	17.12	1.19	2.62	10.0
2036 Launch (6 yr)	13.61	1.68	1.71	6.1
2036 Launch (7 yr)	13.52	1.39	1.88	7.0
2037 Launch	14.40	1.61	1.94	9.7

Low Thrust Transfer Search

The 2036 7 year impulsive trajectory was selected as a baseline and used as an initial guess for the Low-Thrust Interplanetary eXplorer (LInX) tool [11], which uses a Sims-Flanagan [12] transcription of the low-thrust optimization problem with SNOPT [13]. Here, the objective is to arrive at Mercury with sufficient mass to complete the orbital, descent, and landed phases of the mission. The bounded-impulse model and Keplerian propagation used within LInX allows SNOPT to generate a solution quickly and robustly. After generating a solution, we refined the trajectory using direct collocation [14] and implemented the Sun-Probe-Thrust angle path
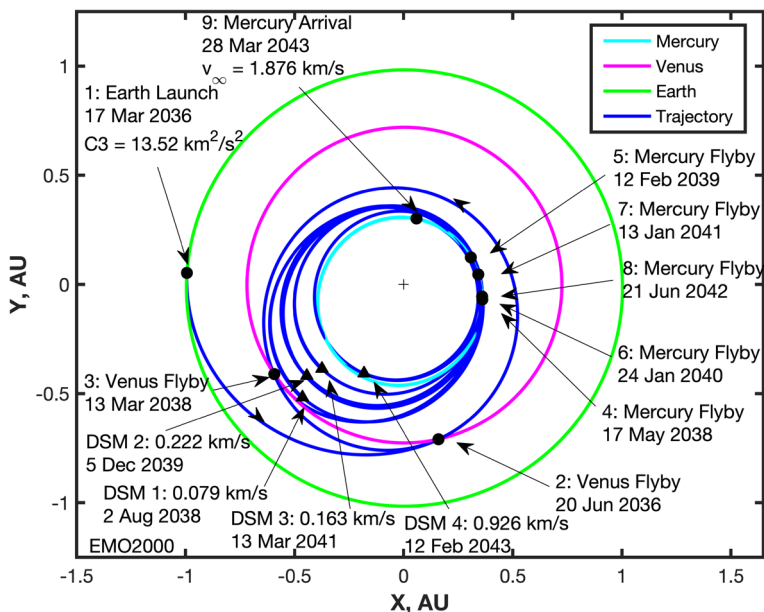
Fig. 5 2036 7 year ballistic transfer case
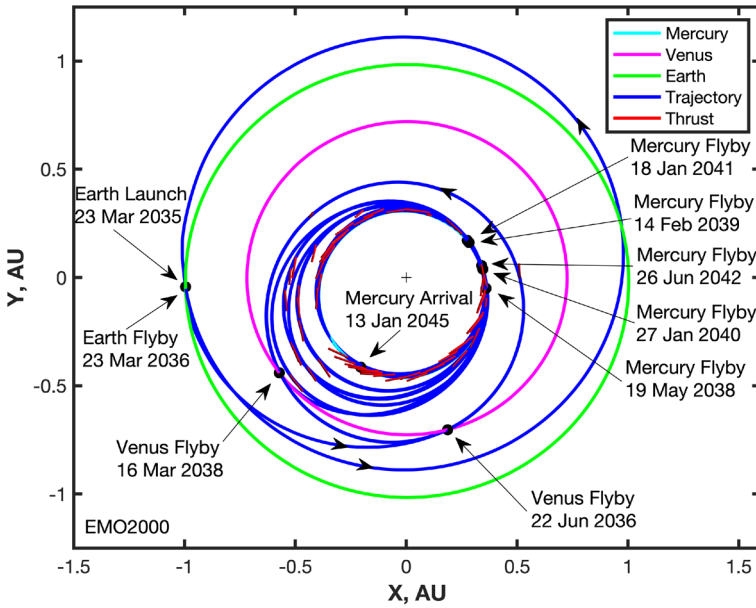
(a) Trajectory to Mercury in Sun-centered EMO2000 frame.
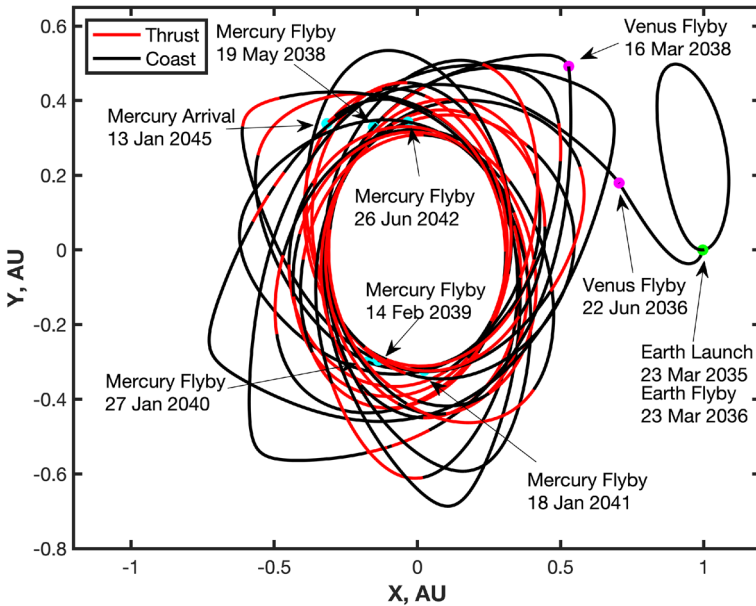
(b) Trajectory to Mercury in Sun-Earth rotating frame.

Fig. 6 Low-thrust trajectory to Mercury launching in 2035. Initial Earth gravity assist included and Sun-Probe-Thrust angle constraint = ± 10°

constraint. We found collocation to be more suitable at enforcing the Sun-Probe-Thrust angle path constraint as the partial derivatives are less coupled than in the Sims-Flanagan formulation, making the problem less sensitive.

Following many design iterations with the larger study team, we settled on a final arrival mass of 8922 kg. To ensure excess mass capability, the baseline solution within the primary launch window is capable of delivering 8944 kg. The arrival date was selected to be Jan 13 2045 based on the phasing of Mercury's local night and the landing site's visibility to Earth for communications. The Falcon Heavy Expendable launch vehicle was selected based on the lift mass requirements. The optimizer minimizes launch mass overall while satisfying the launch vehicle's lift-mass capability for the given trajectory's departure energy (C3). We reserved 470 kg in excess launch capability for the launch vehicle adapter and 10% of the remaining capability to aid subsequent construction of a launch period.

After settling on the 2036 solution as our baseline, a 2035 departure scenario was also created to serve as the primary launch opportunity. In this case, the spacecraft launches into a near-Earth resonant orbit with a period of one year. Then, an Earth gravity assist is used near the 2036 launch date to adjust the spacecraft's outgoing v-infinity to the required vector for the next leg of the trajectory. The 2035 launch case solution is shown in Fig. 6 and the mission itinerary is presented in Table 2. The gravity assist periapsis altitudes are presented along with the post-event heliocentric inclination in the EMO2000 frame. Eclipses are present during Event #'s 4, 5, and 7 with a duration of 20 minutes, 12 minutes, and 15 minutes, respectively. We note that at this stage of the design process, certain operational constraints were not taken into account in the interplanetary trajectory design. This includes enforcing coast arcs before/after gravity assists and evaluating swingbys for superior solar conjunctions.

The series of MGAs and low-thrust VILMs lower the spacecraft's aphelion to match Mercury. However after the last MGA, significant propellant expenditure is required to properly phase and rendezvous with Mercury. This is due to a slight offset

Table 2 2035 scenario trajectory events

| Event #	Description	Body	Epoch	Mass (kg)	V_∞ (km/s)	Alt. (km)	Incl (deg)
1	Launch	E	Mar 23 2035	9406	3.84	–	0.03
2	GA	E	Mar 23 2036	9406	3.84	16988	1.65
3	GA	V	Jun 22 2036	9406	7.42	2476	3.39
4	GA	V	Mar 16 2038	9397	7.53	1576	6.44
5	GA	M	May 19 2038	9392	5.90	200	7.00
6	GA	M	Feb 14 2039	9380	5.17	426	7.00
7	GA	M	Jan 27 2040	9330	3.91	200	7.00
8	GA	M	Jan 18 2041	9324	3.62	1228	7.00
9	GA	M	Jun 26 2042	9245	2.51	200	7.00
10	Arrival	M	Jan 13 2045	8944	0.00	–	–
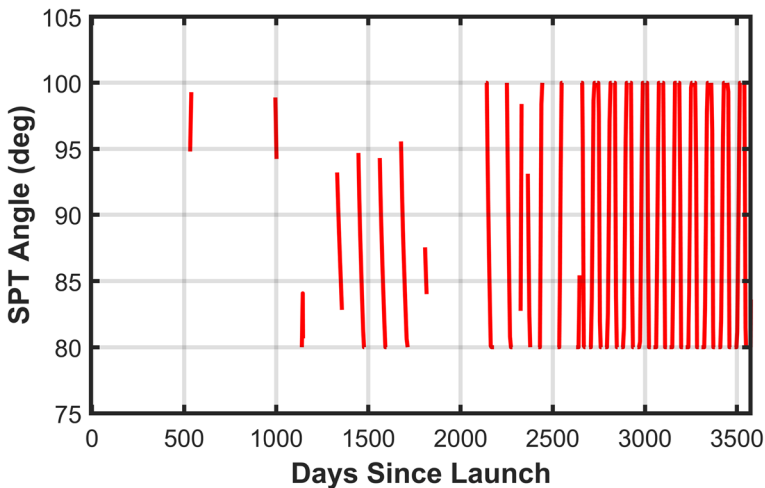
Fig. 7 Sun-Probe-Thrust angle throughout the baseline 2035 launch scenario

in the line of apsides following the last MGA and amplified by the enforced Sun-Probe-Thrust angle constraint, as shown in Fig. 7. Most of the plane change required to orbit match with Mercury is performed by the early gravity assists in the flyby sequence instead of out-of-plane thrusting, as described in Table 2 and shown in Fig. 8. Most thrusting occurs in the spacecraft velocity or anti-velocity direction. The total cruise flight time is longer than both Messenger and BepiColombo at almost 10 years. Two and a half years are spent trying to orbit match with Mercury after the last flyby. This process requires more time than the BepiColombo mission because the delivered mass for orbit, descent, and landing stages are very large.

One challenging aspect of this design problem is the limitation on available power, despite Mercury's close proximity to the Sun. The long mission duration and solar irradiation results in significant solar array degradation. The degradation was modeled using MESSENGER mission flight data [15]. After the MESSENGER mission, JHU/APL developed new analytical techniques [16] and pre-flight conditioning methods for the Parker Solar Probe mission [17] that reduce high intensity/high temperature induced UV degradation. These preconditioning methods reduce the degradation assumed for the Mercury Lander solar array, so the MESSENGER experience bounds the losses. Additionally, the intense thermal environment requires the arrays to be off-pointed for temperature maintenance. As a result, large solar arrays are needed for the interplanetary trajectory. The 2035 launch scenario was used to size the power system since solar array degradation increases with the added year of flight time. The baseline power at 1 AU was designed to be as small as possible to minimize this array size. We elected to use a single NEXT-C electric propulsion system (with one redundant thruster) operating at a baseline power of 9 kW for the interplanetary cruise phase. The power generation and consumption for the 2035 launch case are shown in Fig. 9. This includes 10% margin for contingency operations and to acknowledge the hardware design uncertainty in this early phase concept
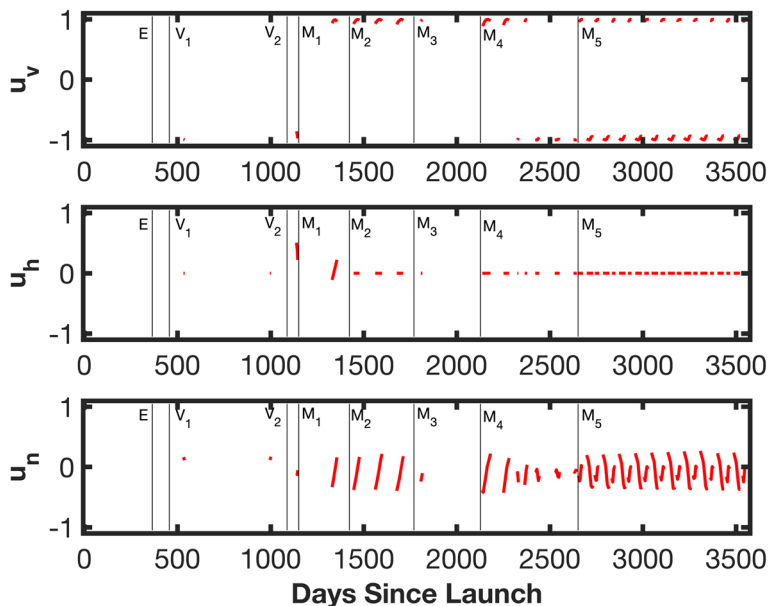
Fig. 8 Thrust profile in the velocity oriented local frame. V points along the velocity, H is in the angular momentum direction (orbit-normal), and N completes the right-handed system to point near the radial direction. Gravity assists included

study. The available power decreases to account for the commanded solar array off-pointing, which reaches approximately 75° at perihelion. Periodic variations in power generation also occur early in the mission and correspond to the spacecraft's orbital distance relative to the Sun varying between gravity assists.

Mercury Orbital Phase

Once at Mercury, the spacecraft must transfer into an orbit from which it can begin its descent to the target landing site. Several constraints were imposed on the landing region, with the most critical being the presence of low-reflectance material, marked as blue surface features in Fig. 10. The most prevalent areas with this material are in the southern hemisphere, between -30° and -60° latitude. Additionally, the landing needs to occur within 5 degrees of the terminator to provide sufficient lighting conditions for landing and science observations without overheating the spacecraft. Two large fields exist at approximately 30° E longitude and 175° E longitude and served as suitable candidates. The arrival year determines which region is more feasible for landing. From 2037 through 2043, landing at 30° E provides more favorable orbit phasing and earth communications, but by 2044 the optimal landing region drifts toward 175° E. For a 2045 arrival, the nominal landing area was selected to be approximately -40° latitude, 178° E Longitude.
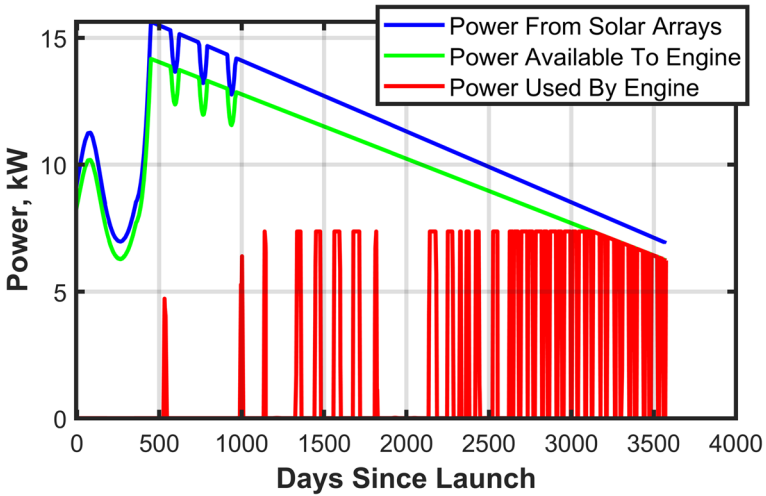
Fig. 9 Power generation and consumption throughout the baseline 2035 launch scenario

The primary constraints on the orbital phase arise from the intense thermal environment near the Mercury surface, particularly on the Sun facing side. The point closest to the Sun on Mercury's surface is known as the sub-solar point. When the spacecraft passes over this region at a low altitude, there is significant reflective heating from Mercury, especially if there are large solar arrays. The solar heating varies throughout Mercury's orbit, with the most intense period at perihelion. Based on these sources, we placed a requirement on the orbital phase stating that the spacecraft shall never pass over the sub-solar point at an altitude less than 200 km near Mercury's perihelion. This constraint was specifically for if the SEP solar arrays were present during the orbital phase.
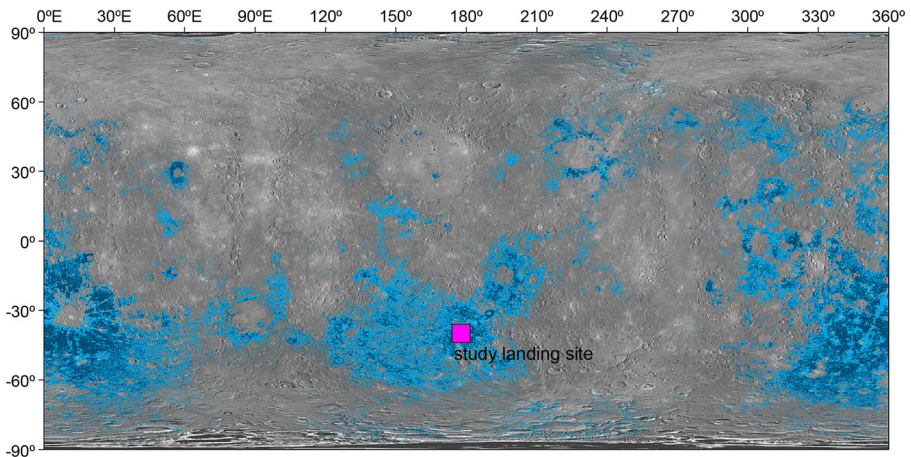

**Fig. 10** Low reflectance regions on the Mercury surface [18]

We studied the use of the SEP system for orbit lowering and maintenance during this phase. Given the altitude constraint over the sub-solar point and desire for surface mapping, a Sun-Synchronous Orbit (SSO) is a favorable choice. However, as shown by Anderson et al. [19], an SSO is not possible at Mercury for the low-specific accelerations provided by our SEP system, owing to our large spacecraft mass. Our next approach was to use a near-polar orbit whose right ascension lines up with the terminator when Mercury passes through perihelion and aphelion, thus ensuring the spacecraft does not encounter the sub-solar point during perihelion. High-fidelity Q-Law [20, 21] simulations were used to rapidly generate spiral trajectories from Mercury capture to the parking orbit and then down to the surface for descent. However, given the large spacecraft mass, the specific acceleration provided by the EP system was very small. This resulted in unreasonably long flight times to transfer from the parking orbit to the low altitude descent orbit. During these transfers, the spacecraft is exposed to the sub-solar point at very low altitudes, violating our requirement.

To overcome the long flight time to reach the descent orbit, we next explored a hybrid system that uses EP to achieve a thermally safe parking orbit and then leverages chemical thrusters for the remaining low-altitude maneuvers. This approach combines the benefits of a high I_{sp} SEP system and the impulse-like maneuver capability of a conventional chemical system, thus saving propellant during orbit lowering and quickly departing the thermally safe parking orbit for the descent orbit.

Given Mercury's small orbital radius from the Sun, the spacecraft requires constant thermal shielding in the Sun direction. This places the same strict pointing constraints on the Sun-Probe-Thrust angle. At perihelion and aphelion, the spacecraft's near-polar orbit can be designed to allow for continuous thrusting without violating this constraint. However, as Mercury's progresses through its orbit, the Sun-Probe-Thrust angle constraint is active for significant portions of the spacecraft orbit period, reducing the effective thrust duty-cycle. This limitation drastically increases the spiral time to the parking orbit and adds years to the total mission duration. Sample spiral trajectories for this case are shown in Fig. 11.

Given these challenges, we selected an all-chemical system for the orbital phase. After the interplanetary SEP system orbit matches with Mercury, it is jettisoned and a Mercury Orbit Insertion (MOI) stage delivers the spacecraft into a thermally safe 100 x 6000 km altitude near-polar parking orbit. The argument of perigee and longitude of the ascending node for the spacecraft's parking orbit were selected so that its periherm occurs at the same latitude as the proposed landing site. The spacecraft has a direct line of sight to the Earth during MOI, and the orbital plane is nearly along the terminator, ensuring no eclipse periods occur around the maneuver. For our final solution, the MOI maneuver occurs on January 13, 2045.

Following orbit insertion, as Mercury's orbit progresses about the Sun, the first crossing of the sub-solar point occurs on February 11, 2045, at approximately 0.38 AU, Mercury true anomaly 264°. When Mercury approaches perihelion, the spacecraft orbit has precessed into a near terminator orientation and no eclipses are encountered. Eclipses can be challenging because the available power is reduced due to thermal off-pointing of the solar arrays. Eclipse periods begin on March 2nd and extend through April 4th.
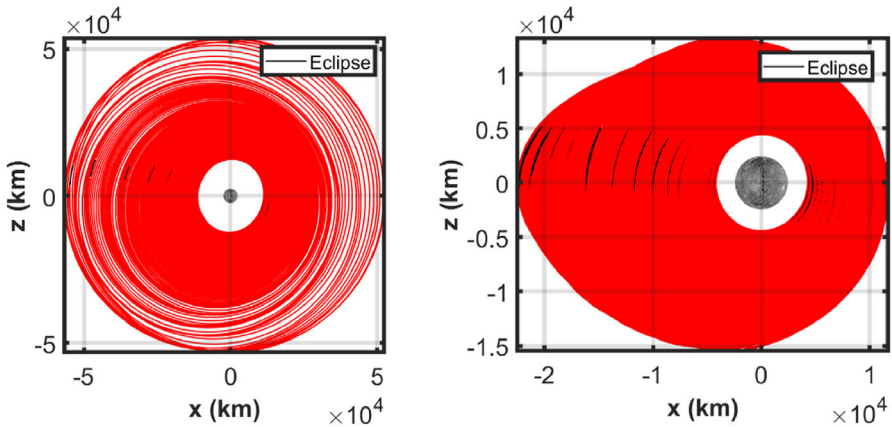
(a) 50k x 50k km to 10k x 10k km orbit transfer. Requires 700 days and 425 kg propellant.

(b) 2k x 20k km to 2k x 2k km orbit transfer. Requires 1300 days and 600 kg propellant.

Fig. 11 Sample Mercury low thrust spiral trajectories

The MOI stage contains a camera with a ±45° articulated field-of-view, which allows for multiple view directions and Sun angles of the notional 150 km circular proposed landing area. The landing site can be imaged between February 11 through March 22nd for a total duration of over 76 hours. This allows the scientists to determine the best landing location with an 8 day period before an apoherm lowering maneuver. This time allows for modifications of the location and parameters of the descent maneuver.

Thermal requirements limit the apoherm lowering maneuver to occur at a Mercury true anomaly greater than 130°, which occurs on March 28th. The maneuver was chosen to occur on March 30, 2045, to allow sufficient time for possible maneuver adjustments to re-target the nominal landing as additional navigation data is received. At this point the orbit apoherm is lowered to 2000 km. A landing date of April 12th, 2045, was selected because it is 10 days into the first contact window between April 2nd through May 4th, 2045, allowing margin for landing epoch changes depending on the image campaign. On the landing date, the MOI stage lowers periherm to 20 km, resulting in a 20 km x 2000 km orbit. Once in this orbit, the MOI stage is jettisoned, leaving the descent and landing stages. The orbital phase trajectory is shown in Fig. 12.

Descent and Landing

The landing site imaging while in the 100 x 6000 km altitude orbit will occur at a resolution of a few meters per pixel. While this is too coarse for definitive selection of a landing site, it is expected to provide enough information to down-select kilometer size landing areas that meet scientific criteria and provide low-level identification of ground hazards. After the apoherm lowering maneuver into the 100 x 2000 km
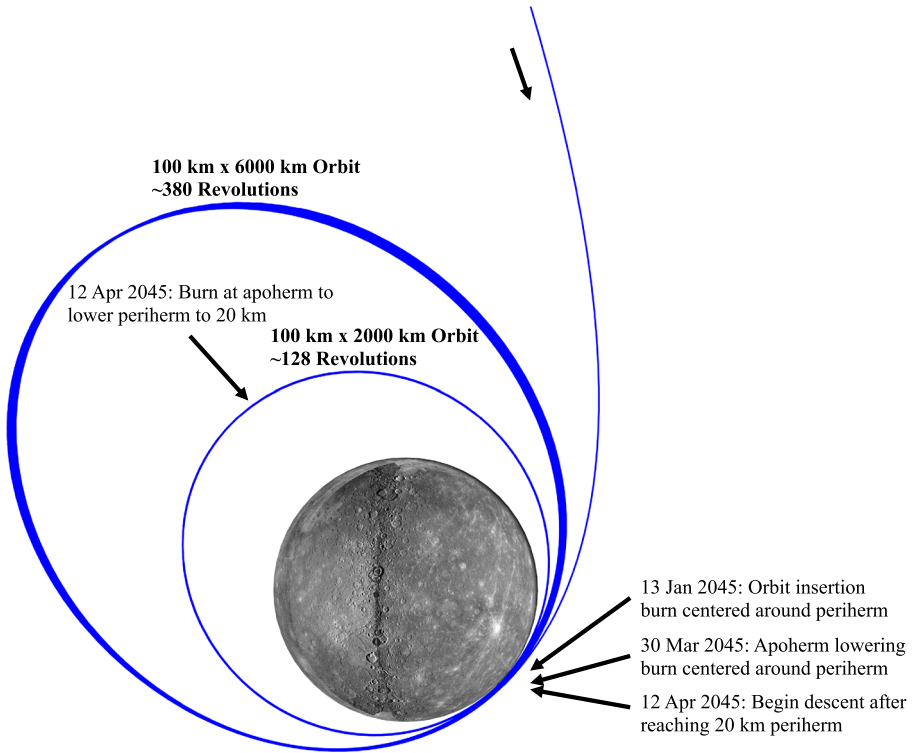
Fig. 12 Mercury Lander orbital phase

orbit, the orbit is phased to place the periherm at the interface point for the landing sequence, 150 km ahead of the landing area. During this time, enough tracking data is collected to prepare the final targeting sequence that lowers the periherm altitude to 20 km and eject the MOI stage prior to the landing sequence start.

The descent and landing follow the same approach as developed for prior lunar landing concepts [22, 23], as illustrated in Fig. 13. The descent stage leverages a STAR 48 GXV solid rocket motor (SRM) to reduce spacecraft energy, and the liquid propulsion system (LPS) on the lander provides more maneuverability and removes the remaining energy for a soft landing.

The landing sequence begins with a braking burn executed by the solid rocket motor for an estimated 75 sec, decelerating the Lander from a 3.395 km/s incoming horizontal speed at periherm to a nearly vertical 83 m/s by the end of the burn. The braking burn is followed by a 30 sec coast arc, during which the descent stage is jettisoned and a landing site is determined using a scanning LIDAR and an on-board hazard map generated from collected data. The near vertical motion achieved at the end of the braking burn allows for a continuous scan of a single landing area during the coast arc. An initial landing site is selected at roughly 3.1 km altitude. Following this coast arc, the guidance system targets the selected landing site during the liquid burn while continuing to refine the selection with increased resolution on descent.
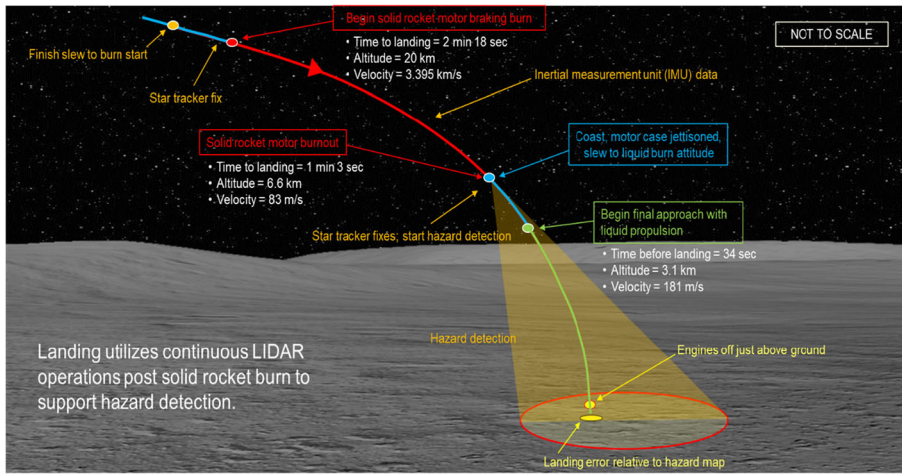
Fig. 13 Landing sequence

The landing sequence was designed using a simple targeting scheme. We determined a range of altitudes for which a (near) vertical descent could be possible with a minimum coast arc duration based on the assumed lander propulsion system capabilities. A 3-segment attitude profile for the SRM burn was used to target those altitudes while achieving near zero horizontal speed. The resulting descent profile is shown in Fig. 14. This approach was selected over an optimizer for early stage development to easily adapt to changing system designs. This method also allows for simple hazard avoidance using a vertical descent over a limited scanning area for LIDAR processing.

The SRM burn was simulated with a nonlinear thrust profile similar to that provided in [23] but adapted to the available test data from the GXV ground testing. The attitude profile consists of 3 segments: a short segment to provide an initial descent speed, a second segment to provide a fixed gravity offset and maintain the initial
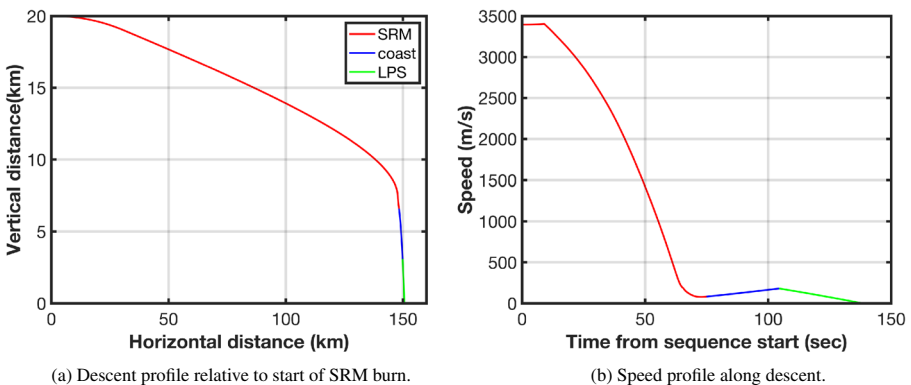

(a) Descent profile relative to start of SRM burn.

(b) Speed profile along descent.

Fig. 14 Descent and landing trajectory

descent speed through most of the burn, and a final segment to maximize energy decrease by thrusting in the anti-velocity direction. The first segment is parameterized by time, the second segment is parameterized by the gravity offset and duration, and the last segment is predetermined from the state of the spacecraft. In addition, a time offset was added to the SRM model during the design iterations.

The selected profile only involves pitch control and is achievable through thrust-vector control of the SRM, with the remaining attitude control performed with small liquid thrusters. The short duration of the burn allows for attitude estimates to be performed on inertial measurement units from the most recent star tracker measurements and uploaded state knowledge prior to the burn ignition. The coast arc provides the necessary buffer to evaluate the SRM performance and adjust the final descent.

With the vertical descent profile, the LIDAR measurement processing is assumed to provide translational state corrections in addition to terrain assessment via frame registration. Depending on the scanning LIDAR frequency and other performance parameters seen on current LIDAR units, estimates of a 500 m x 500 m search area with pixel covering between 0.53 m^2/px to 0.1 m^2/px and a few centimeter range accuracy are achievable by the start of the burn. This accuracy is sufficient to generate a hazard map and select a landing site within the search area that maximizes the distance from a given rock size or a given slope value. Additional LIDAR measurements will focus on the search area and should result in hazard detection with cm-level accuracy.

The liquid descent was simulated with a 91% throttle assumption to account for variability and margin for lateral control. The remaining 9% thrust can produce more than 3kN in lateral force, or accelerations larger than 4 m/s^2, allowing the lander to reach any lateral coordinate in the hazard map within the first 15 sec of the descent. Navigation during the final descent is performed relative to the hazard map generated during the coast arc (3.1 km altitude), and LIDAR measurements can be used to provide meter-level navigation accuracy within the map.

This descent approach builds on the development of the Moon lander and assumes similar terrain/rock sizes as the Moon landings, where 10 m x 10 m areas free of typical hazards (e.g. 25 cm rocks or slopes steeper than 10 deg) are highly likely to be found within the search area. Similar to Moon landers, the final <100 m of the descent would be performed on inertial measurement unit data only, to avoid dust lofting interference on the optical sensors. This drives the landing accuracy to a few meters from the selected site. The 620 kg lander will touchdown on April 12 2045, and ground operations will last until the Sun rises again on July 11, 2045, roughly 13 weeks. The lander has direct-to-Earth communication availability for up

Table 3 Mercury Lander ΔV Budget

Mission Phase	ΔV (m/s)	I_{sp} (s)	Propellant (kg)
Cruise	2025	4100	462
Orbital	867	277	2050
Descent	3300	308	2824
Landing	316	277	80

to 7 weeks during the ground operations period. The associated science instruments and measurements are consistent with this mission life and downlink availability. The mission will end after sunrise when the thermal conditions at the landing site exceed spacecraft tolerances.

A summary of the ΔV budget for the full mission is shown in Table 3. The values for the cruise and orbital phases do not include propellant margins that were added in for the final design, and the descent and landing ΔV are adjusted for gravity losses. A 6% and 2.7% margin was used for the cruise and orbital phases, respectively. These are discussed in more detail in the final Mercury Lander report.

Conclusion

The Mercury Lander Mission Decadal Survey serves as a preliminary design study for a lander to explore the low-reflectance material that exists on the surface of Mercury. The mission design is heavily constrained by the extreme thermal environment at low solar ranges and near to Mercury's surface. For the interplanetary transfer, we selected a SEP design that leverages a series of Venus and Mercury gravity assists. Accounting for solar array mass and complexity, we selected a single NEXT-C thruster operated at up to 9kW at 1 AU launching on a fully expendable Falcon Heavy launch vehicle.

Both chemical and SEP systems were considered for the orbital phase. Despite the propellant savings associated with the electric propulsion approach, the orbit lowering transfer times were unreasonable and violated thermal constraints. As a result, we selected a chemical system to perform orbit insertion and lowering.

Descent and landing operations are performed using a solid rocket and liquid propulsion hybrid system. Onboard LIDAR measurements are prioritized, as compared to a Moon lander, given the lack of a detailed terrain map. This allows for the refinement of a coarse landing area from orbit down to an actual landing site during the descent. Touchdown will occur near dusk on Mercury, and ground operations extend until the Sun rises on the landing site approximately 13 weeks later.

Though challenging, this analysis demonstrates that a Mercury Lander can be feasibly accomplished using existing technologies. Additional technology developments in the next decade may offer improvements, but we don't expect any dramatic changes in the basic architecture. The overall system mass is dominated by propellant (hydrazine, xenon, and solid rocket). Increased I_{sp} for any of these would benefit the overall fuel fraction, owing to the exponential nature of the rocket equation. Higher thrust EP could reduce the overall time-of-flight by perhaps a year. There is limited benefit from more capable launch vehicles, since higher launch mass equates to a higher requirement on the SEP thrust capability. While it may be feasible to use a SLS class vehicle to launch an all-chemical implementation, we would still view this design as inferior to the hybrid option. Perhaps the most significant improvement would be solar array technologies that could efficiently operate face-on in the solar environment at Mercury. Though we are unaware of any such development, such a technology would reduce the size of the SEP stage arrays and could possibly eliminate the orbital stage altogether.

References

1. Peplowski, P.N., Evans, L.G., Hauck, S.A., McCoy, T.J., Boynton, W.V., Gillis-Davis, J.J., Ebel, D.S., Goldsten, J.O., Hamara, D.K., Lawrence, D.J., et al.: Radioactive elements on Mercury's surface from MESSENGER: Implications for the planet's formation and evolution. Science **333**(6051), 1850–1852 (2011)
2. Ernst, C., Chabot, N., Klima, R., Kubota, S., Byrne, P., Hauck, E.A.S.A.: A Mercury Lander Mission Concept Study for the Next Decadal Survey, 51st Lunar and Planetary Science Conference (2020)
3. Yen, C.-W.L.: Ballistic Mercury orbiter mission via Venus and Mercury gravity assists. J. Astronaut. Sci. **37**, 417–432 (1989)
4. Langevin, Y.: Chemical and solar electric propulsion options for a Cornerstone Mission to Mercury. Acta Astronautica **47**(2-9), 443–452 (2000)
5. McAdams, J.V., Dunham, D.W., Farquhar, R.W., Taylor, A.H., Williams, B.G.: Trajectory design and maneuver strategy for the MESSENGER mission to Mercury. J. Spacecraft Rock. **43**(5), 1054–1064 (2006)
6. Casalino, L., Colasurdo, G., Rosa Sentinella, M.: Low-thrust trajectories to mercury with multiple gravity assists 43rd AIAA/ASME/SAE/ASEE Joint Propulsion Conference & Exhibit (2007)
7. Jehn, R., Schoenmaekers, J.: Bepicolombo Trajectory Options to Mercury in 2016 and 2017 24th International Symposium on Space Flight Dynamics (2014)
8. Lantukh, D.V.: Preliminary design of spacecraft trajectories for missions to outer planets and small bodies. PhD thesis The University of Texas at Austin (2015)
9. Lantukh, D.V., Russell, R.P., Campagnola, S.: Automated inclusion of v-infinity leveraging maneuvers in gravity-assist flyby tour design. Adv. Astronaut. Sci. **143**(II), 865–884 (2012)
10. Hauck, S.A., Eng, D.A., Tahu, G.J.: Mercury Lander Mission Concept Study. The National Academies, USA (2010)
11. Ozimek, M.T., Riley, J.F., Arrieta, J.: The Low-Thrust interplanetary explorer: a Medium-Fidelity algorithm for Multi-Gravity assist Low-Thrust trajectory optimization, AAS space flight mechanics conference, no. AAS 19–348 (2019)
12. Sims, J.A., Flanagan, S.N.: Preliminary design of Low-Thrust interplanetary missions, AAS/AIAA astrodynamics specialist conference, girdwood, alaska, no AAS 99–338 (1999)
13. Gill, P.E., Murray, W., Saunders, M.A.: SNOPT: An SQP algorithm for Large-Scale constrained optimization. SIAM Rev. **47**(1), 99–131 (2005)
14. Patterson, M.A., Rao, A.V.: GPOPS-II: A MATLAB Software for solving multiple-phase optimal control problems using hp-adaptive Gaussian quadrature collocation methods and sparse nonlinear programming. ACM Trans. Math. Softw. (TOMS) **41**(1), 1–37 (2014)
15. Gallagher, D.: MESSENGER Solar array operations and flight data Space Power Workshop (2014)
16. Stall, R., Schurman, M., Sulyma, C.M., Gerger, A., Gaddy, E.: UV Degradation of space solar cell assemblies under high temperature and irradiance. In: 2018 IEEE 7th World Conference on Photovoltaic Energy Conversion (WCPEC)(A Joint Conference of 45th IEEE PVSC, 28th PVSEC & 34th EU PVSEC), IEEE, pp. 3339–3343 (2018)
17. Driesman, A., Ercol, J., Gaddy, E., Gerger, A.: How the Parker Solar Probe Survives Close Encounters With the Sun (2019)
18. Klima, R.L., Denevi, B.W., Ernst, C.M., Murchie, S.L., Peplowski, P.N.: Global distribution and spectral properties of low-reflectance material on Mercury. Geophys. Res. Lett. **45**(7), 2945–2953 (2018)
19. Anderson, P., Macdonald, M., Yen, C.-W.: Novel orbits of Mercury, Venus and Mars enabled using low-thrust propulsion. Acta Astronaut. **94**(2), 634–645 (2014)
20. Petropoulos, A.: Low-thrust Orbit Transfers using Candidate Lyapunov Functions with a Mechanism for Coasting. AIAA/AAS Astrodynamics Specialist Conference and Exhibit 748–762 (2004)
21. Petropoulos, A.E.: Refinements to the Q-law for the low-thrust orbit transfers. AAS/AIAA Space Flight Mechanics Conference, Copper Mountain CO (2005)

22. Parker, J.S., McElrath, T.P., Anderson, R.L., Sweetser, T.H.: Trajectory Design for MoonRise: A Proposed Lunar South Pole Aitken Basin Sample Return Mission. J. Astronaut. Sci. **62**(1), 44–72 (2015)
23. Ozimek, M.T., McGee, T.G.: Near-Optimal Guidance for precision lunar landing with a combined solid rocket motor and liquid propulsion system. 14-387 AAS/AIAA space flight mechanics conference, santa fe NM (2014)